Optical Engineering

SPIEDigitalLibrary.org/oe

Validation of atmospheric propagation models in littoral waters

Arie N. de Jong
Piet B. W. Schwering
Alexander M. J. van Eijk
Willem H. Gunter

SPIE

Validation of atmospheric propagation models in littoral waters

Arie N. de Jong
Piet B. W. Schwering
Alexander M. J. van Eijk
Organisation for Applied Scientific Research
P.O. Box 96864
The Hague, The Netherlands
E-mail: anejdejong@hetnet.nl

Willem H. Gunter
Institute for Maritime Technology
Simon's Town 7995, South Africa

Abstract. Various atmospheric propagation effects are limiting the long-range performance of electro-optical imaging systems. These effects include absorption and scattering by molecules and aerosols, refraction due to vertical temperature gradients and scintillation and blurring due to turbulence. In maritime and coastal areas, ranges up to 25 km are relevant for detection and classification tasks on small targets (missiles, pirates). From November 2009 to October 2010 a measurement campaign was set-up over a range of more than 15 km in the False Bay in South Africa, where all of the propagation effects could be investigated quantitatively. The results have been used to provide statistical information on basic parameters as visibility, air-sea temperature difference, absolute humidity and wind speed. In addition various propagation models on aerosol particle size distribution, temperature profile, blur and scintillation under strong turbulence conditions could be validated. Examples of collected data and associated results are presented in this paper. [DOI: 10.1117/1.OE.52.4.046002]

Subject terms: atmospheric transmission; refraction; turbulence; scintillation; atmospheric blur; beam wander; marine boundary layer.

Paper 121557P received Oct. 25, 2012; revised manuscript received Mar. 4, 2013; accepted for publication Mar. 5, 2013; published online Apr. 8, 2013.

1 Introduction

The range performance of electro-optical sensors is generally determined by three major contributors: the signature of the target (size, shape, and reflection) and its background (radiance distribution), the characteristics of the intervening medium (transmission, refraction, blur, and scintillation) and the sensor parameters (sensitivity, resolution). For most of these issues, models have been developed, predicting ranges for a variety of weather conditions and locations. In this paper, characteristics of atmospheric propagation effects will be discussed, especially for littoral waters. In coastal and maritime locations, the uncertainty of the model predictions increases due to the long horizon distances and the poor availability of basic atmospheric parameters. In practical applications, such as detection and classification of small boats from a coastal location or from a tall ship, identification at the longest possible ranges is required (for example 3×3 m targets at 25 km).

Atmospheric propagation models are available for most topics: extinction due to aerosols and molecules, refraction due to temperature gradients in the vertical direction and turbulence. For maritime conditions, locally measured particle size distributions (PSD) are used,[1] from which scattering is calculated via Mie calculations, included in the MODTRAN transmission code.[2] In coastal areas, the PSD may be disturbed by breaking waves in the surf zone, creating additional large particles, influencing the wavelength dependent scattering. By using a retrieval method, based upon data from a path-averaging multiband transmissometer, it should be possible to obtain more detailed information on the real PSD characteristics. Refraction effects, responsible for distortion of the atmospheric point spread function (PSF) and variations of the optical horizon range, follow from the Monin-Obukhov (MO) boundary layer theory,[3] predicting vertical profiles and implemented in the turbulence and refraction model over the sea (TARMOS) code, developed at TNO. These profiles can be implemented in ray tracing schemes, providing the angle of arrival (AOA), under which a distant source is observed. The MO theory, based upon atmospheric input parameters as wind speed, relative humidity, air temperature, sea temperature and air pressure, also predicts C_n^2, the structure parameter for refractive index, describing turbulence effects such as scintillation and blur. Quantitative measurement of these effects as described by the theory (Andrews[4]), was one of the major issues during the experiments. As a result of the blur data, range performance can be predicted for given target and sensor characteristics (Holst[5]).

For the validation of these models it is highly recommended to arrange an experiment covering a long period with a variety of weather conditions. Moreover it is essential that the main wind direction is coming from the open ocean. The location of the selected validation campaign, called False Bay atmospheric experiment (FATMOSE) is indicated in Fig. 1, showing the range of 15.7 km between the Institute of Maritime Technology (IMT) in Simon's Town and the National Sea Rescue Institute (NSRI) in Strandfontein.

Sensors were located at IMT at 14.5 m above mean sea level (AMSL) and Roman rock lighthouse (RRL) at 15 m AMSL (9 m for the visibility meter). The sources were mounted on the roof of NSRI at different heights: 9.7 and 5.8 m for the two central sources and 8.7 m AMSL for the two outer sources. The mean weather characteristics in the False Bay, as collected by the weather stations at IMT and RRL during the FATMOSE trial from November 2009 to October 2010, are shown in Fig. 2.

0091-3286/2013/$25.00

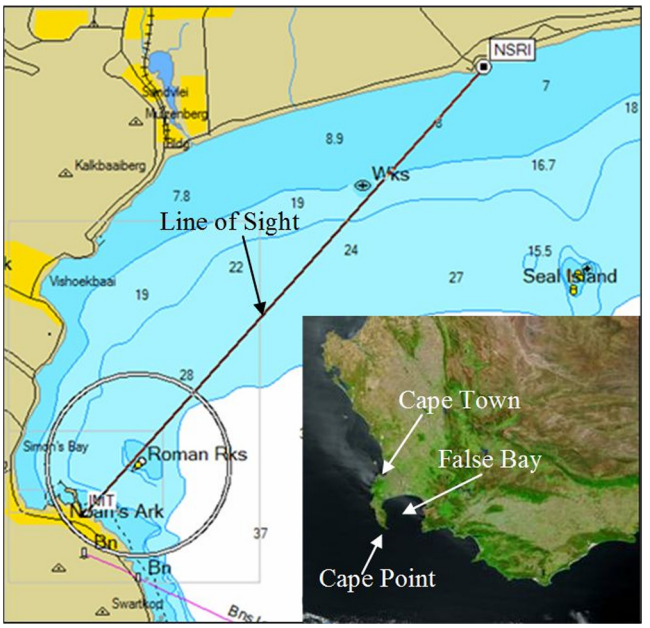

Fig. 1 Location of the FATMOSE trial in the False Bay (South Africa).

Figure 2 shows a large variability in the visibility with a mean value of 15 km, about the length of the measurement path. This value, measured locally at RRL with a Vaisala FS11 visibility meter, is a perfect distance for PSD retrieval studies carried out with the multiband transmissometer, located at IMT. It is also shown that wind speeds up to 20 m/s may occur from a dominating southeastern direction (from the open ocean). Statistics on the air sea temperature difference (ASTD), having an impact on the behavior of C_n^2, are also shown in Fig. 2, where it is noted that the water temperature was measured radiometrically at RRL. The ASTD values were ranging from roughly -4 to $+8$ K, introducing various temperature profiles. From buoy measurements and satellite imagery it was found that the water temperature in the Bay is not constant, mainly due to the mixing of warm and cool currents in the area. As a consequence, it is very likely that the ASTD is not constant along the path. Other parameters such as air temperature, relative humidity, and wind speed were found to be very similar at the two weather stations (at IMT and RRL).

The mean value of C_n^2, as measured between IMT and RRL (range 1.8 km) with a Scintec BLS 900 scintillometer, was found to be 10^{-15} $m^{-2/3}$, which is significantly lower than for land conditions where values of 10^{-14} and higher are commonly measured.

The plots in Fig. 2 illustrate the attractiveness of the False Bay location for atmospheric propagation experiments

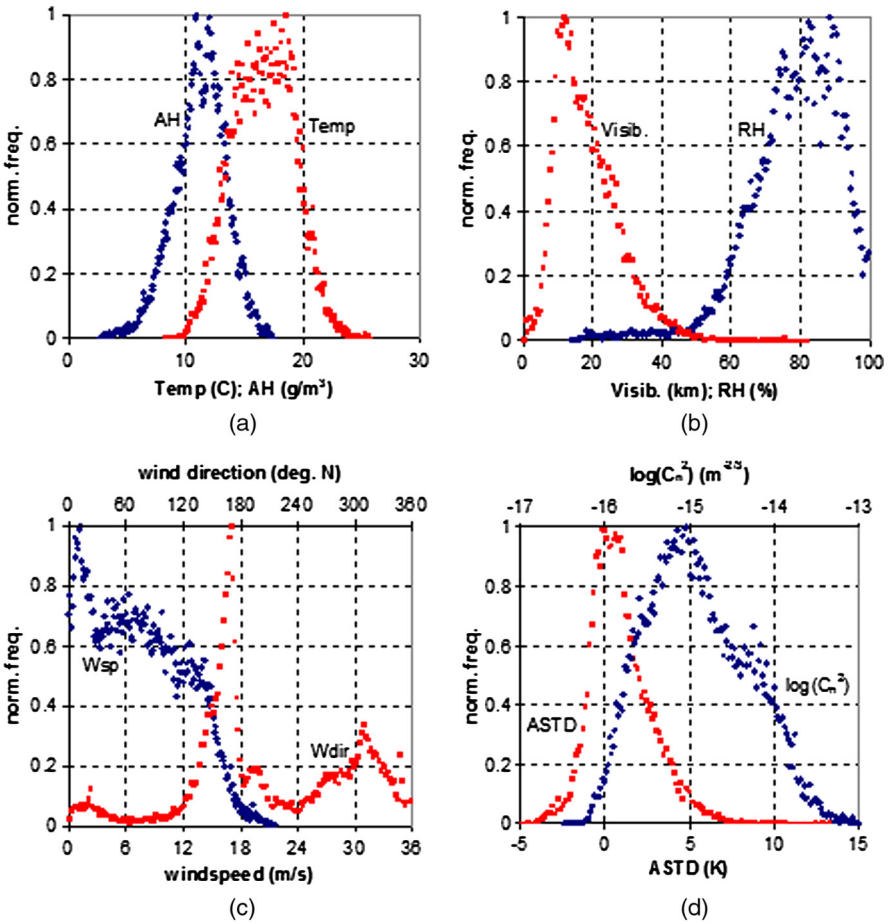

Fig. 2 Review of the mean weather statistics in the False Bay area during FATMOSE. (a) Absolute humidity (AH) and air temperature. (b) Visibility and relative humidity (RH). (c) Wind speed and wind direction. (d) Air-sea temperature difference (ASTD) and C_n^2.

thanks to the fact that the campaign could be run for a period of more than 10 months. This allows the selection of intermediate periods with "good" weather with stable conditions for at least several hours where the validation of propagation models can be carried out in a successful manner. Detailed descriptions of the set-up of FATMOSE and results of the various investigations have been presented in several SPIE conference papers. In the paper on transmission[6] a new method for the retrieval of aerosol PSDs has been introduced, based upon multiband transmission data. The paper on refraction contains a comparison of measured angle of arrival (AOA) with predictions via ray tracing through MO theory based vertical temperature profiles.[7] Atmospheric blur,[8] directly related to the target identification range, was shown to be smaller than expected from former coastal C_n^2 data. For scintillation[9] a comparison of measured data with predictions from the strong turbulence theory was made, due to the longer range used in FATMOSE, where the weak turbulence theory is no longer valid. In this paper, a summary of the main validation results, including their theoretical background, as discussed in these papers is given. In addition, long term statistics are presented of the transmission levels in various spectral bands, as well as the statistics of blur and scintillation, being of importance for operational purpose.

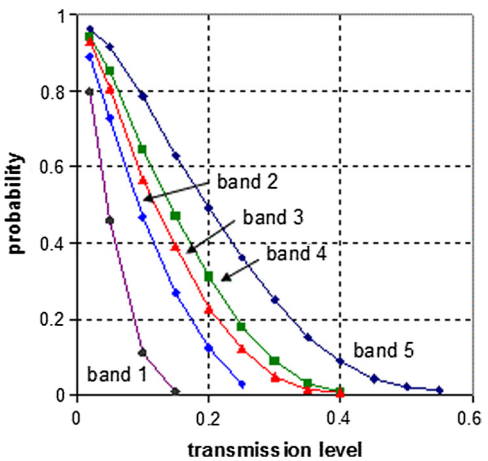

Fig. 3 Statistics of the (total) transmission levels during 230 days of measurements for the five spectral bands of the MSRT system.

2 Transmission and Aerosol Retrieval

The MSRT transmissometer, developed at TNO, provides transmission data in five spectral bands, ranging from 0.40 to 0.49 μm (band 1), 0.57 to 0.65 μm (band 2), 0.78 to 1.04 μm (band 3), 1.39 to 1.67 μm (band 4) and 2.12 to 2.52 μm (band 5). The source has a diameter of 20 cm and is modulated with a frequency of 1000 Hz. At the receiver, with an aperture of 4 cm, the integration time was set to 21 s for transmission purpose and 10 ms for scintillation, with a sampling time of 5 ms. The first issue, being of importance for operational use, concerns the long-term transmission statistics in each of the five bands, which is shown in Fig. 3. This figure shows quantitatively the benefit of using sensors operating at longer wavelengths. The reason for this effect is, of course, the decrease of the aerosol particle density with particle diameter, as shown in Ref. 1, resulting in less scattering for longer wavelengths.

This is precisely the basic idea for using the MSRT in the determination of the PSD. In this investigation, the generally accepted PSD, as discussed[1] and based upon three or four lognormal neighboring components, is approached by a well-known Junge distribution with one lognormal component for particles smaller than 0.16 μm and with a maximum for a particle diameter of 0.08 μm. The Junge distribution is given by $\log(\mathrm{d}N/\mathrm{d}D) = J_c + J_e \cdot \log(D)$ or $\mathrm{d}N/\mathrm{d}D = 10^{J_c} \cdot D^{J_e}$, in which D is the particle diameter (in μm) and $\mathrm{d}N/\mathrm{d}D$ the number of particles per μm per cm^3. For a Junge coefficient, $J_c = 2$ and two Junge exponents $J_e = -3.5$ and -4.5, distributions are shown in Fig. 4(a). Considering Beer's law, $\tau = \exp(-\sigma R)$, where τ is the transmission for the path length R (15.7 km) and σ the extinction coefficient (km^{-1}), we can convert this into $\log\{-\ln(\tau_i)\} = \log(15.7\sigma_i)$, where τ_i and σ_i deal with the i'th waveband. For the centers of the five MSRT wavebands, $\log(15.7\sigma_i)$ was calculated for a number of Junge exponents, J_e between -3 and -5, using a standard Mie code for the extinction coefficient of spherical particles (pure water).[10] The result of this calculation is shown in Fig. 4(b) for $J_e = -3.5$ and -4.5 and $J_c = 0$. It is noted that in a real atmosphere, water can be contaminated, introducing a complex index of refraction which may lead to deviating (stronger) Mie extinctions at certain wavelengths, which are neglected here because of the broad spectral bands.

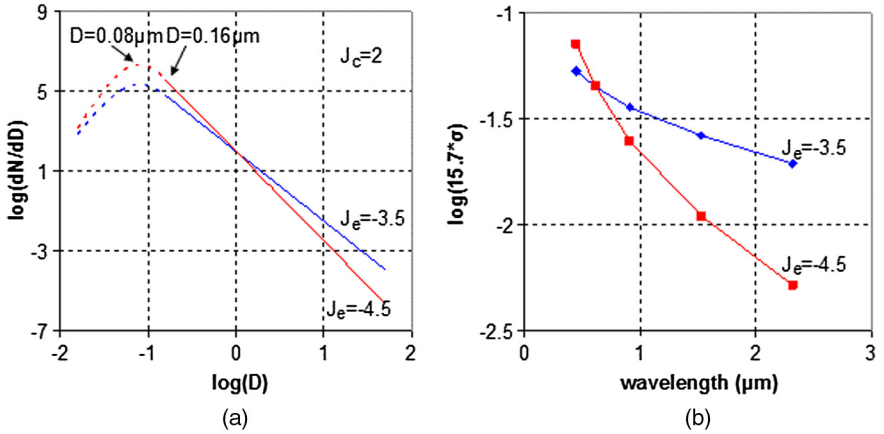

Fig. 4 Characteristics of the adopted Junge particle size distribution for two values of J_e and $J_c = 2$ (a). In (b) the corresponding aerosol extinction as function of wavelength is shown for two values of J_e, $J_c = 0$ and a range of 15.7 km, as calculated with the Mie code.

If the plotted curves are approximated by straight lines, it is found that the slope s of these lines varies with J_e in a nearly linear way, as shown in Fig. 5(a), for the case of three selected wavelengths. The regression line for three wavelengths is found to be $J_e = 2.54s - 2.84$ and for the five wavelengths $J_e = 2.85s - 2.82$, so the measurement of s directly delivers J_e. In order to obtain J_c, it has to be realized that variation of J_c results in a vertical shift of the plots in Fig. 4(b) according to $\log(15.7\sigma_i) + J_c$. The values of $\log(15.7\sigma_i)$ were calculated with the Mie code as function of J_e. The results for three of the MSRT waveband centers are shown in Fig. 5(b), where it appears that the plots fit perfectly with third order polynomials, such as $\log(15.7\sigma_i) = 0.042{J_e}^3 + 0.6983{J_e}^2 + 3.723J_e + 4.8317$ for band 3 (0.91 μm). When these five (or three) values of $\log(15.7\sigma_i)$ are compared with the measured values of $\log\{-\ln(\tau_i)\}$, it is realized that J_c is just the difference between both.

It is noted that this method of determination of J_e and J_c fails if the transmission level is too low (<0.02) or too high (>1), such as occurring in cases of refractive gain[6] (Fig. 13). It is further noted that the transmission levels as discussed before are considered to be just due to the extinction by aerosols. A correction has to be made to the measured total transmission levels τ_{tot}, realizing that $\tau_{\text{tot}} = \tau_{\text{mol}}\tau_{\text{aer}}$, where τ_{mol} and τ_{aer} are representing the transmission by molecules and aerosols, respectively. The total transmission data are therefore divided by the molecular transmission in order to obtain the transmission by aerosols only. For each of the spectral bands, the molecular transmission for the path length of 15.7 km is approximated via a linear relationship with AH (absolute humidity) deduced from MODTRAN. For example, for band 3 (around 0.91 μm) is found $\tau_{\text{mol}} = -0.0072\text{AH} + 0.754$; AH is related to the relative humidity RH and the air temperature $T(C)$ by $\text{AH} = (0.02T^2 + 0.1874T + 5.5304)\text{RH}/100$. These relations are valid for the domain of AH as occurring in the False Bay (5 to 15 g/m^3).

In Fig. 6, plots are shown of the transmissions in bands 2 and 4, including the retrieved associated values of J_c and J_e for a 2.5 days period in which the wind speed decreases and the visibility increases on the 31st of January around 13.00. At this time, the slope s is increasing, resulting in a decrease of J_e and J_c. It is noted that the total transmission was about 0.27 for band 2, which corresponds to a visibility of 47 km. This value corresponds quite well with the measured (local) visibility of 40 km at RRL.

In addition to the data in Fig. 6, a selection of six periods of about five days was made where the weather conditions did meet the requirements (no rain, fog or refraction). For all data of these days, retrieved J_e and J_c data were correlated with the transmission levels, of which the result is shown in

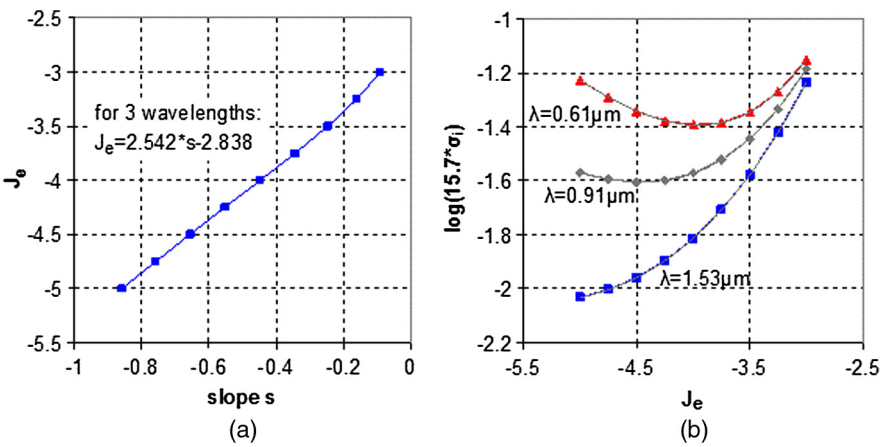

Fig. 5 Junge exponent J_e as function of the slope s in the plot of the extinction $\log(15.7\sigma)$ versus wavelength (a). Plots of $\log(15.7\sigma_i)$ versus J_e, supporting the J_c retrieval for three wavelengths, being the centers of bands 2, 3, and 4 are shown in (b). J_c is obtained by comparing $\log(15.7\sigma_i)$ with $\log\{-\ln(\tau_i)\}$ for the three (or five) MSRT wavebands.

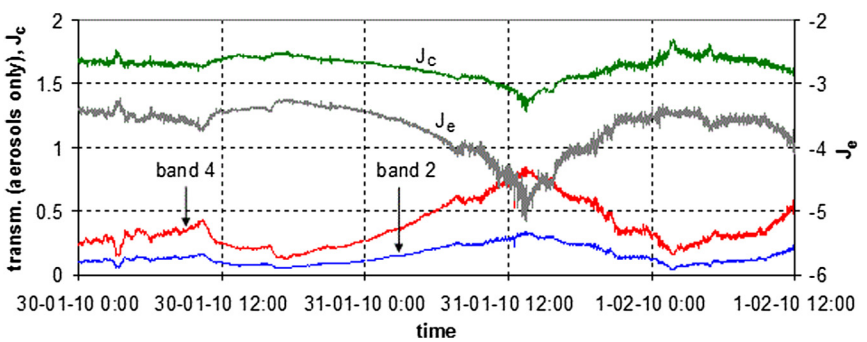

Fig. 6 Transmission plots for the MSRT spectral bands 2 and 4 during 2.5 days. From the slope s of $\log(15.7\sigma)$ (where σ is the extinction coefficient) versus the wavelength, values of J_e and J_c were retrieved, showing variations in the particle size distribution.

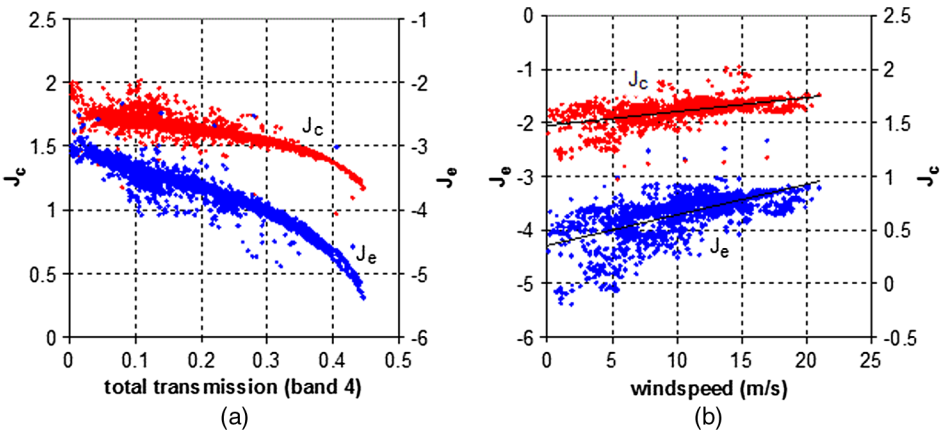

Fig. 7 Plots showing a decrease of J_e and J_c with increasing total transmission (a) and an increase with increasing wind speed (b) for 29 days of transmission data. Increase of J_e and J_c implies bigger particles with a higher concentration, as can be expected with rough seas or decreasing visibility.

Fig. 7(a). Despite some sudden changes in wind direction during the selected periods from southeast to northwest (or vice-versa) introducing different air masses, the correlation is remarkably good both J_e and J_c decrease for higher transmission levels (band 4). It is interesting to note the increase of J_e and J_c with wind speed as shown in Fig. 7(b), as expected from the MODTRAN model. In this case, only data with values for relative humidity RH smaller than 80% were taken. In a similar plot an increase of J_e and J_c with RH (for wind speeds less than 10 m/s) was found.

3 Refraction

Atmospheric refraction is a well-known phenomenon, frequently visible near sunrise and sunset and showing distortions of the sun disc. The reason for this effect is the presence of a gradient in the refractive index of air in the lower part of the boundary layer. Consequently, rays bend upward when the air is cooler than the water and bend downward when the air is warmer than the water. Optically this means that the horizon is observed under a lower angle with the tangent to the earth in the first case and a higher angle in the second case. During the FATMOSE experiment, a fixed source at NSRI was constantly observed with a Topcon theodolite coupled to a CCD camera. By means of special analysis software, the AOA (angle between the source and the geometrical horizon) was determined ten times per minute. This AOA can also be calculated if the vertical profile of the refractive index (or temperature) is known, as shown before.[11] The related ray-tracing program is based upon calculation of the ray curvature K_c at a number of points along the ray via $K_c = (\mathrm{d}n/\mathrm{d}z)/n$, where n is the refractive index and z is the altitude (in m) above water. Following Beland,[12] n is approximated by $n = 1 + 786 \cdot 10 - 8P/T$ where P is the barometric pressure (in $\mathrm{N/m^2}$) and T the air temperature (K). The derivative follows from $\mathrm{d}n/\mathrm{d}z = -(\mathrm{d}T/\mathrm{d}z + 0.0348) \cdot 786 \cdot 10 - 9 \cdot P/T^2$, where the value of 0.0348 results from the pressure decrease with altitude.

Three examples of temperature profiles and their derivatives are shown in Fig. 8(a) for an ASTD of −2 K. One profile follows from the turbulence and refraction model over the sea (TARMOS) code, which is based upon the MO theory,[3] and developed at TNO. This profile $T_z - T_0 = -0.1513 \cdot [\ln(z/0.000021) - 2 \cdot \ln\{0.5(1+(1+15z/352)^{0.5})\}]$ and its derivative $\mathrm{d}T/\mathrm{d}z$ is associated with a wind speed of 15 m/s and a relative humidity of 70%. These parameters, together with two air temperatures, one at water level and one at a standard height and the air pressure are input parameters for the TARMOS code.[7] They basically determine the vertical exchanges of heat, moisture and momentum in the marine boundary layer. The other two profiles are basically power profiles, defined by $T_z - T_0 = Bz^A$

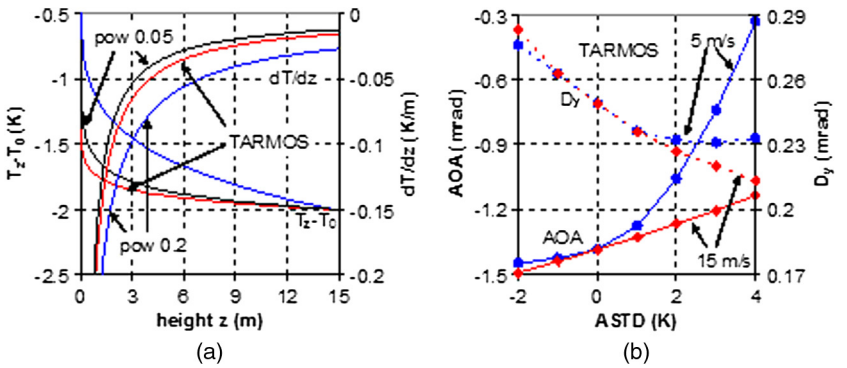

Fig. 8 Vertical profiles of the temperature and the temperature gradient for two power law profiles and one predicted from TARMOS (ASTD = −2 K @ z = 15 m, wind speed 15 m/s) (a). Predictions of the angle of arrival AOA and the differential angle of arrival D_y versus ASTD for the profiles, predicted from TARMOS for wind speeds of 5 and 15 m/s (b).

determined by the two parameters A and B. In our example of ASTD equaling −2 K, we take for the exponent A 0.2 and 0.05 and for the constant B, respectively −1.167 and −1.747. In the ray-tracing program, an additional term for the adiabatic temperature decrease with altitude is always added to these profiles, specifically $-0.006z$.

In the ray-tracing program, a step size of 10 m was chosen, taking into account K_c at each point and the earth radius. In this way the arrival height and the angle between the ray and the tangent to the earth after each step are calculated, which are used as input for the next step. Ray-tracings were carried out for a set of TARMOS profiles with ASTD running from −2 to +4 K and two wind speeds 5 and 15 m/s, resulting in AOA values as shown in Fig. 8(b). For the receiver and source, height was taken 14.5 m, respectively 8.7 m above mean sea level (AMSL). Figure 8(b) also shows predictions of D_y, which is the angular distance between two sources at 9.7 and 5.8 m AMSL. The plots show that for positive ASTDs, the wind speed plays a key role on the temperature profile from TARMOS, creating larger gradients at lower altitudes as a consequence of the MO theory. This effect is not occurring in the simple power profile for T. It is noted that TARMOS is just using simple bulk input parameters air- and sea temperature, relative humidity, wind speed and air pressure, governing the exchanges of heat, momentum and moisture in the boundary layer. In Fig. 9, two examples are shown of measured AOA and D_y together with the associated ASTD for "perfect" days.

"Perfect" days means days without big changes in wind speed, wind direction, relative humidity and air pressure and without rain or fog. In the left example of Fig. 9, the wind was variable from the north, in the right example the wind speed was about 10 m/s, blowing from the southeast. More examples are shown.[7] Most of them show a good match of AOA and $-5D_y$, which corresponds to the prediction of Fig. 8(b). Examples are also shown of big variations in AOA due to conditions of large ASTD ($> +5$ K),[7] in which the horizon is elevated up to 0.8 mrad. Examples are shown of refractive gain conditions in the transmissometer data,[6] when ASTD is negative. In this case, transmission levels >1 may occur and occasionally mirages may be observed. For the period 1 to 6 February, plots of AOA versus ASTD and of D_y versus AOA are shown in Fig. 10.

The plots in Fig. 9 show a relation between AOA and ASTD of 50 to 60 μrad per degree, corresponding to the TARMOS prediction in Fig. 8. The plots in Fig. 10 became very scattered due to the "nonperfect" weather in the days before 6 February. For this reason it was decided to make a selection of 230 data points (hourly averaged) along the FATMOSE period. Plots for these data points, similar to those in Fig. 10, are shown in Fig. 11. In the case of the selected data, the range of ASTD values is bigger than for 1 to 6 February, which allows a better validation of the TARMOS prediction. For the TARMOS prediction, also shown in Fig. 11, an average wind speed of 10 m/s and a relative humidity of 80% was taken, resulting in the polynomial approximation $\mathrm{AOA} = 0.00006x^3 + 0.0068x^2 + 0.0618x - 1.386$ (x = ASTD). The correspondence between measurement and prediction is quite good, better than the relation between D_y and AOA, where the measured D_y values are about 15 μrad bigger than the predicted ones. It is noted that for all AOA, a downward correction of 66 μrad was applied due to the local horizon tilt at IMT by the gravity effect of the nearby mountain.

4 Scintillation

Scintillation is the atmospheric propagation effect, resulting in signal fluctuations of a small target at long range, generally described by the scintillation index (SI), defined as $(\mathrm{std}/\mathrm{avg})^2$, where std and avg are the standard deviation and the mean value of the signal. The magnitude of SI is dependent on the turbulence strength, for which C_n^2 is used and defined via the structure function $D_n(r) = C_n^2 r^{2/3}$, where r is the distance between two points, at which the refractive index n of the air is correlated.[4] C_n^2 can be predicted from the MO theory, or measured indirectly from sonic anemometer data or via the measurement of SI. An important issue is the relation between SI and C_n^2, for which the weak turbulence theory has been developed, predicting $\mathrm{SI} = 1.23 C_n^2 (2\pi/\lambda)^{7/6} R^{11/6}$,[4] with λ as wavelength and valid for point sources and receivers. Measurements have shown that for values greater than 1.2, SI is saturated (constant with increasing C_n^2). For the FATMOSE range of 15.7 km, this means that for $C_n^2 > 2 \times 10^{-16}$ m$^{-2/3}$ such sensors cannot be used for SI measurements. Therefore, large aperture scintillometers were used during FATMOSE, such as the Scintec BLS 900 and the MSRT transmissometer, similar to the suggestion by Ting.[13] As a consequence, the

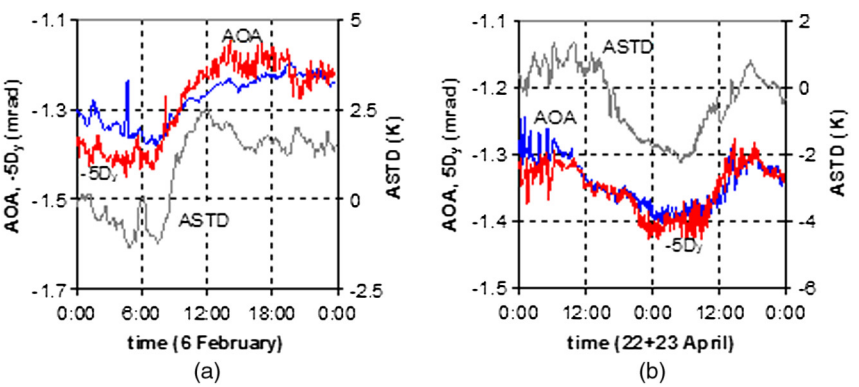

Fig. 9 Examples of measured refraction data (angle of arrival AOA and the differential angle of arrival D_y), showing the correlation with the air to sea temperature difference ASTD for two periods, 6 February (a) and 22 to 23 April (b).

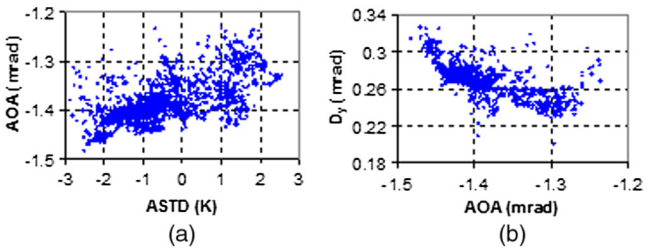

Fig. 10 Correlation between the angle of arrival AOA and the air to sea temperature difference ASTD (a), and the differential angle of arrival D_y and AOA (b) for the refraction data of 1 to 6 February. In both plots the correlation coefficient is about 0.50, which is low due to some "nonperfect" weather moments in the measurement period.

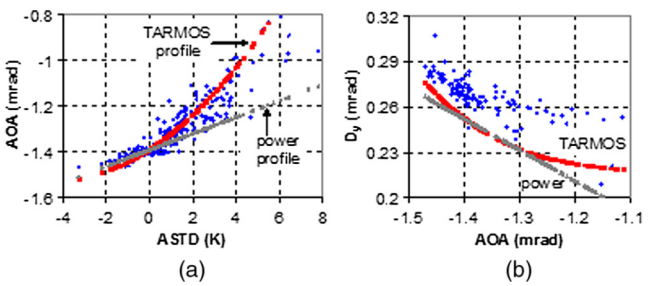

Fig. 11 Correlation plots as in Fig. 11 for a selection of 230 hourly averaged data series in comparison with predictions, based on the TARMOS and the power temperature profile. Both 11(a) with AOA versus ASTD and 11(b) with D_y versus AOA show that the TARMOS based prediction gives a better correspondence with the measured data.

signals did not show saturation effects as illustrated in Fig. 12(a), showing a histogram of 4200 data points (channel 4) under strong scintillation conditions. The plot shows nicely the well-known log-normal distribution, as proposed in the theory of Rytov.[4]

The prediction of C_n^2 from the MO theory, as applied in the TARMOS code, is based upon the knowledge of scaling parameters for wind speed, temperature and humidity, u_*, T_*, and q_*, which determine indirectly the Obukhov length L (m). This parameter is roughly related to ASTD for a wind speed of 5 m/s, $1/L = 0.02\text{ASTD (K)}$. For wind speeds less than 4 m/s, L is dropping rapidly. Knowledge of T_* and L allow the approximation of C_T^2, the structure parameter for temperature, which is directly linked with C_n^2 via $C_n^2 = \{(n-1)/T\}^2 C_T^2$, where T is the absolute temperature (K).[12] The sonic anemometer delivers wind speed in three orthogonal directions together with the air temperature in a data rate of 100 samples per second. The covariance of the fluctuations of the wind speed in vertical direction w and the fluctuations of the wind speed in the main wind direction u, $\langle wu \rangle$, delivers by definition $-u_*^2$. T_* follows from $T_* u_* = -\langle wt \rangle$, where t stands for the temperature fluctuations. Similar to the TARMOS calculation, C_T^2 can be obtained and thus C_n^2. It is clear that in all these calculations several assumptions and approximations are made. One of them is the spectrum of the fluctuations, for which basically the spatial spectrum from the Kolmogorov theory is taken.[4] This predicts on a log-log scale for the one dimensional spectrum a drop of the amplitude with $\kappa^{-5/3}$, where κ is the spatial frequency. Figure 12(b) shows that this prediction is nearly correct for both strong and weak scintillation conditions.

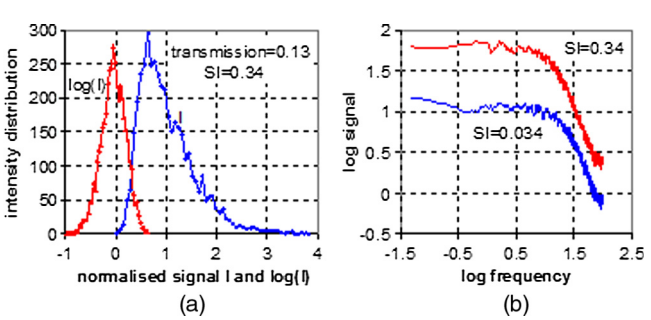

Fig. 12 (a) Histograms of the intensity I and $\log(I)$ for 21 s of MSRT data for a case of strong scintillation index (SI = 0.34). (b) Shows Fourier spectra of MSRT data for weak (0.034) and strong SI (0.34). All data are taken in spectral band 4.

It is noted, however, that these spectra are taken from temporal MSRT signals. This can only be explained by Taylor's hypothesis,[4] based upon the assumption that crosswinds are blowing the turbulence structure unchanged through the line of sight. A deviation of Kolmogorov is found in the position of the knee in the spectrum, which is occurring at 10 Hz, while the theory assumes 1 Hz.

A comparison of C_n^2 measurements and predictions and ASTD is shown in Fig. 13 for two periods in April. These time plots show that the trends of C_n^2 follow reasonably well the predictions via ASTD, but that deviations occur in the various sources of C_n^2, probably due to inhomogeneities along the path. It is also found that SI values of 0.01 and less have been measured, indicating that C_n^2 values far below 10^{-16} $\text{m}^{-2/3}$ occur in the False Bay area, which is below the range of the BLS scintillometer.

The conversion of measured SI values to C_n^2 follows from the strong turbulence theory.[4] Andrews derives an equation for the aperture averaging factor A, defined as the ratio of SI for aperture D and (SI_R) for aperture zero. The factor A is depending heavily on SI_R and the parameter $(\pi D^2)/(2\lambda R)$, where D is the diameter of the aperture and $(\lambda R)^{0.5}$ represents the Fresnel scale, related to the first Fresnel zone, determining the intensity of an incoming wave front at range R. Plots of A as function of D are shown in Fig. 14(a) for a number of C_n^2 values, $\lambda = 0.8$ μm and $L = 15.7$ km. A appears to be less than 0.2 for $D = 20$ cm, which is further illustrated in Fig. 14(b), where A is plotted as function of C_n^2 and D as parameter.

Actually, aperture averaging occurs for the source (Celestron 9 cm, MSRT 20 cm) and for the receiver (Celestron 20 cm, MSRT 4 cm). The two different aperture averaging factors have to be multiplied. It is, therefore, interesting to compare SI values of both instruments, such as shown in Fig. 15(a), where for the MSRT, channel 3 has been taken which has about the same waveband as the Celestron. It is noted that MSRT data in the morning hours from 10 to 12 o'clock have been removed due to sun glint effects in the sea. Both data series correlate quite well with a correlation coefficient of 0.90. The main reason for the spread in the data is due to the smaller signal to noise ratio of the Celestron data. A rough approximation of the factor A can also be obtained by realizing that inside the aperture D, coherent wave front patches (radius ρ_0) are averaged by the factor D/ρ_0. The spatial coherence width ρ_0

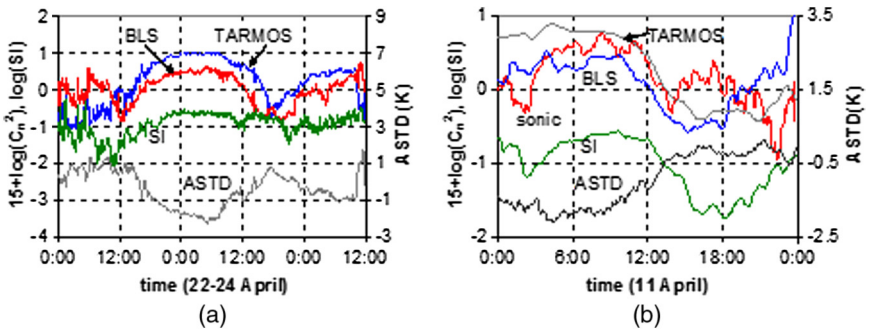

Fig. 13 Plots of measured SI, ASTD and C_n^2 (structure parameter for the refractive index) for 22 to 24 April (a) and 11 April (b) in comparison to C_n^2, predicted from the MO theory based TARMOS code.

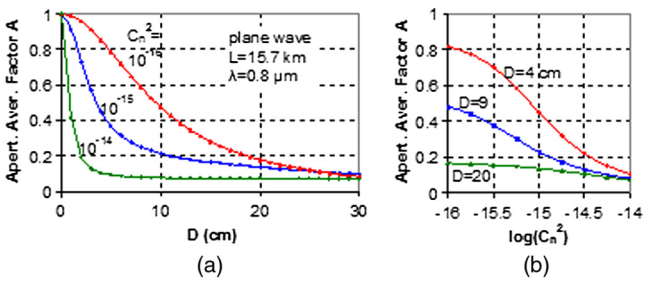

Fig. 14 Aperture averaging Factor A, determining the reduction of scintillation due to increased sensor and receiver apertures, predicted from the strong turbulence theory. (a) A as function of the receiver diameter D and in (b) as a function of C_n^2 $(m^{-2/3})$.

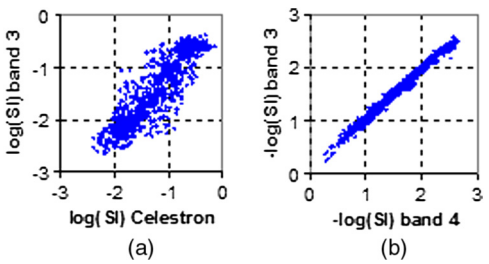

Fig. 15 (a) Comparison of the scintillation index SI for a representative data set, collected by MSRT and Celestron (correlation coefficient 0.90). (b) A similar comparison of SI from different MSRT bands (correlation coefficient 0.99).

is related to C_n^2 by $\rho_0 = \{1.46(2\pi/\lambda)^2 C_n^2 R\}^{-3/5}$, predicting ρ_0 values of a few cm, resulting in aperture averaging A values of 0.1 to 0.2, which corresponds roughly with the previously mentioned prediction.

It was further found that the SI values of the three MSRT bands correlate extremely well and were nearly equal, as shown in Fig. 15(b). This shows that during FATMOSE, scintillation was not originating from small eddies, which create wavelength dependence (as in the SI value for the weak turbulence case[14]). In the False Bay, scintillation occurred rather in the refraction regime. Applying the factor A to the SI data from the MSRT system allows a comparison of its C_n^2 and the C_n^2, measured by the Scintec scintillometer. The result, presented in Fig. 16(a), shows data points for a selected series of 458 events during the FATMOSE period (with "correct" weather). Each event was chosen inside

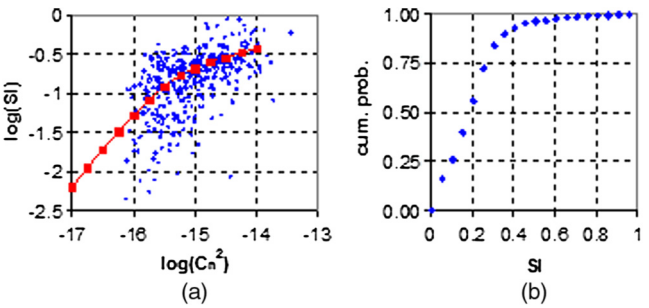

Fig. 16 (a) The dots show a comparison of SI and C_n^2 for a selected data series collected under "correct" weather conditions, measured by the Celestron and the scintillometer, the curve through the squares presents SI, predicted after correction for aperture averaging. (b) Shows the cumulative probability of SI for the whole FATMOSE period.

several hours of constant weather, while averages were taken over a 2-h period.

Both data sets correspond reasonably well for C_n^2 values above 10^{-16} $m^{-2/3}$; the Scintec system is limited to values above 10^{-16} $m^{-2/3}$. The predicted data in Fig. 16(a) are based upon C_n^2 values as low as 10^{-17} $m^{-2/3}$, converted from hypothetical SI data for the MSRT and Celestron systems via the relation $\log(C_n^2) = 0.6623x^4 + 4.2334x^3 + 9.9979x^2 + 11.458x - 10.623$, in which $x = \log(\mathrm{SI})$ based upon the aperture averaging factor A. Figure 16(b) shows a cumulative probability plot of the SI values from the Celestron camera for the same selected data series, where care was taken that the weather statistics were about the same as those in Fig. 2. It is clear that 50% of the SI data is below 0.2% and 90% below 0.4. This means that the magnitude of the atmospheric scintillation over the False Bay area is generally low to moderate.

5 Atmospheric Blur

The main purpose of the Celestron camera, mentioned in the previous section for the collection of scintillation data, was the measurement of the atmospheric line spread function (LSF). The 8-inch telescope with a focal length of 2030 mm, was provided with a 10 bits Marlin F-033B camera with 640×480 pixels, a 30 Hz frame rate and a near-IR cut-on filter. With a pixel size of 5×5 μrad, the total field of view of the camera is 3.2×2.4 mrad. The camera integration time was generally less than 1 ms, with a minimum of 0.1 ms, depending on the actual visibility and illumination

conditions. A series of 150 frames (5 s) were collected every 5 min. Some examples of the Celestron imagery are shown in Fig. 17 with long (9 ms) integration times in conditions of good visibility and low turbulence (a) and two images of the four sources for low (b) and high (c) turbulence conditions. The two central sources are used for measuring the LSF, while the left source (modulated) and right source are used for transmission (MSRT), respectively, refraction (Topcon) measurements.

Figure 17 also shows the LSF $L(x)$ and $L(y)$ in X- and Y-direction for the two images (b) and (c) for low and high turbulence conditions. Both LSFs are found from $L(x) = \int S(x,y)\mathrm{d}y$ and $L(y) = \int S(x,y)\mathrm{d}x$, where $S(x,y)$ is the signal level at position (x,y) in the focal plane above a certain threshold above the mean background level in an area around the spot. It is found that generally the LSFs can reasonably well be approximated by a Gaussian distribution. In each frame, the centers of "gravity" x_c and y_c are obtained from $x_c = \iint xS(x,y)\mathrm{d}x\mathrm{d}y / \iint S(x,y)\mathrm{d}x\mathrm{d}y$ and $y_c = \iint yS(x,y)\mathrm{d}x\mathrm{d}y / \iint S(x,y)\mathrm{d}x\mathrm{d}y$ with mean values for all 150 frames of x_{cm} and y_{cm}. The beam wander BW is defined as the mean value of $\mathrm{BW} = \sqrt{\{(x_{\mathrm{cn}} - x_{\mathrm{cm}})^2 + (y_{\mathrm{cn}} - y_{\mathrm{cm}})^2\}}$ $(n = 1$ to 150). The blur for each frame follows from the second moments M_{20} and M_{02} of $S(x,y)$ in both directions $M_{20} = \iint (x - x_c)^2 S(x,y)\mathrm{d}x\mathrm{d}y / \iint S(x,y)\mathrm{d}x\mathrm{d}y$ and $M_{02} = \iint (y - y_c)^2 S(x,y)\mathrm{d}x\mathrm{d}y / \iint S(x,y)\mathrm{d}x\mathrm{d}y$. The final blur value for each frame σ_t is found from the geometrical average $\sigma_t = \sqrt{(\sqrt{M_{20}}\sqrt{M_{02}})}$ in number of pixels (multiplied with five for blur values in μrad). To obtain the atmospheric blur σa, the system blur σs has to be subtracted quadratically from σ_t: $\sigma_a = \sqrt{(\sigma_t^2 - \sigma_s^2)}$. In the system blur, three contributions are taken into account: the source diameter (5.7 μrad), the pixel size (5 μrad), and the diffraction from the aperture of the telescope (20 cm), resulting in a σ_s value of 2.89 μrad.[8] Finally, the mean value of σ_a is calculated for the 150 frames.

In Fig. 18 the statistics for blur and beam wander are shown for the same selected series as discussed in the previous section, being representative for the year-round conditions in the False Bay. It appears that 50% of the blur and the beam wander is smaller than 20 μrad, respectively, 8 μrad. It is interesting that the distribution of the blur [Fig. 18(a)] is roughly log normal, which is not the case for the beam wander distribution [Fig. 18(b)]. It is noted that the blur values may vary considerably within one series of 150 frames, showing standard deviations of 10%, sometimes 20% to 30% of the mean value. The smallest blur within one series (lucky shot) may be 50% of the mean, but the biggest blur may be twice the mean value. The LSF profiles $L(x) = \exp\{-(x/\sigma_a)^2/2\}$ imply that the atmospheric MTF also has a Gaussian shape, $\mathrm{MTF}_a(f) = \exp\{-2(\pi\sigma_a f)^2\}$, in which f is the spatial frequency (cycles/μrad), which allows a good estimation of the optical resolution for a given blur σ_a.

It is also noted,[15] that two line sources, separated by a transverse distance of $2.43\sigma_a$ (at 15.7 km), are just discernible by a remaining contrast of 10%. Another interesting issue which appeared regularly, was the synchronous beam wander (amplitude and phase) of the upper and lower source, as shown in Fig. 19. It appeared as if the whole image was moving in the same direction with the same amplitude, apparently tilting due to large intermediate eddies. The predicted atmospheric $\mathrm{MTF}_{\mathrm{ap}}$ is according to Fried,[16] $\mathrm{MTF}_{\mathrm{ap}}(f) = \exp\{-(f/f_c)^{5/3}\}$, with the cut-off frequency $f_c = \rho_0/\lambda$ and ρ_0 the transverse coherence width as specified in the previous section $\rho_0 = \{1.46(2\pi/\lambda)^2 C_n^2 R\}^{-3/5}$. This means that $\sigma_a \approx \lambda/(\rho_0\pi\sqrt{2}) = 2.56\lambda^{-0.2}(C_n^2 R)^{0.6}$; with $\lambda = 0.8 \cdot 10^{-6}$ m and $R = 15.7 \cdot 10^3$ m follows: $\sigma_a = 14.0 \cdot 10^9 (C_n^2)^{0.6}$ μrad. For the mean C_n^2 value of 10^{-15} $\mathrm{m}^{-2/3}$, σ_2 becomes 14 μrad, which is reasonably in agreement with the measured values. Beam wander is predicted by the relation given by Beland, $\mathrm{BW} = (2.91 D^{-1/3} C_n^2 R)^{0.5}$. For $D = 0.2$ m and $R = 15.7 \cdot 10^3$ m follows $\mathrm{BW} = 2.8 \cdot 10^8 (C_n^2)^{0.5}$ μrad, resulting in a BW value of 8.9 μrad for a C_n^2 value of 10^{-15} $\mathrm{m}^{-2/3}$, which, again, is close to the observed mean value.

An example of a time plot where blur, BW and SI (measured data from the Celestron camera) correspond reasonably well, is shown in Fig. 20. It is noted that the blur and BW are not becoming extremely small when the C_n^2 value is small. For example, according to the theory, a $C_n^2 = 10^{-16}$ $\mathrm{m}^{-2/3}$ would result in blur and BW values of 3.5, respectively, 2.8 μrad, which have never been measured.

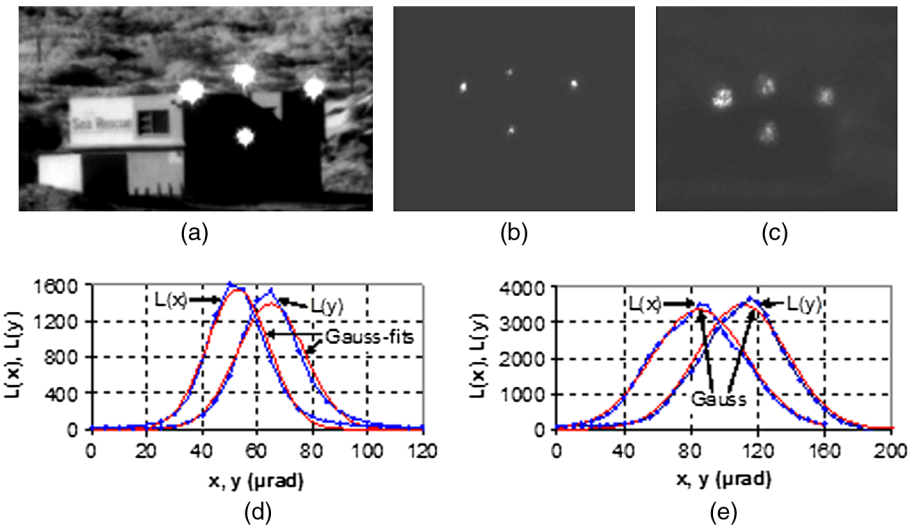

Fig. 17 Impression of the four sources on the roof of the NSRI building (a) and examples of small and large blur conditions [(b) and (c)] with associated line spread functions [(d) respectively (e)].

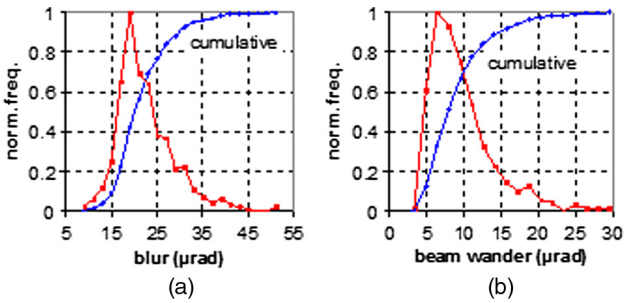

Fig. 18 Normalized histograms of the blur (a) and the beam wander (b) for the selected data series, representative for the year-round FATMOSE period.

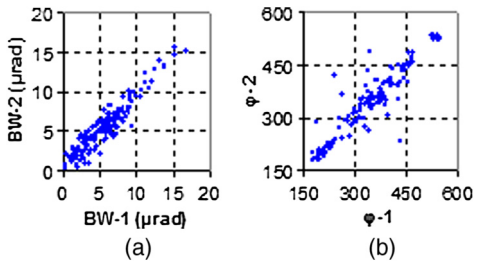

Fig. 19 Correlation of the beam wander for both sources. (a) Shows the amplitude and (b) the direction of motion of the center of gravity of the spot. The angles $\varphi - 1$ and $\varphi - 2$ represent the counter clockwise angles with the positive X-axis $+360$ deg.

On the other hand, a C_n^2 of 10^{-14} $m^{-2/3}$ would result in blur and BW values of 55, respectively, 28 μrad, higher than the maximum measured values. Correlation plots of the blur and BW, and of blur and SI for the measured data, shown in Fig. 20, are presented in Fig. 21, together with theoretical predictions. It appears that the measured blur is considerably bigger than the predicted blur. It is noted that for the prediction of C_n^2, the conversion is made again from the measured SI via the polynomial approximation between SI and C_n^2, mentioned in the previous section. From this relation, σ_a is calculated via the blur equation, given before. A similar result of a too large measured blur for blur values <20 μrad is found in the analysis of the blur and BW data of the selected data series, as mentioned before.

This is shown in Fig. 22(a), where the prediction is based upon the Scintec C_n^2 value and the σ_a equation. It might be that the theory on ρ_0 and its implication on σ_a is not correct

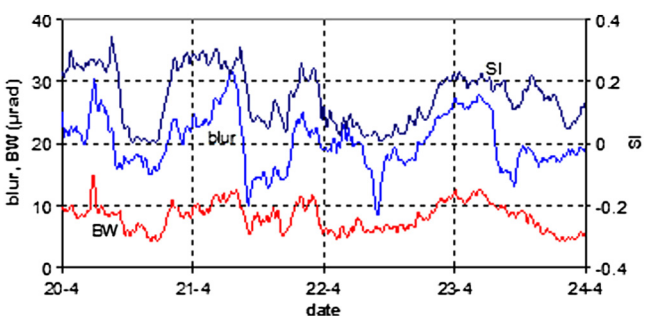

Fig. 20 Four days of recording of blur, beam wander and scintillation index, as collected with the Celestron camera, showing temporal correlations.

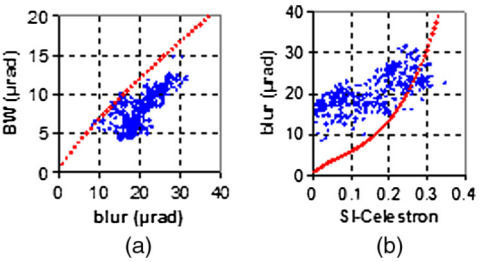

Fig. 21 The dots in (a) present the correlation the between blur and beam wander and in (b) the correlation between the blur and SI for the measured data shown in Fig. 20. The dotted curves in both plots present predictions from C_n^2 values, obtained via the polynomial approximation between C_n^2 and SI from the strong turbulence theory.

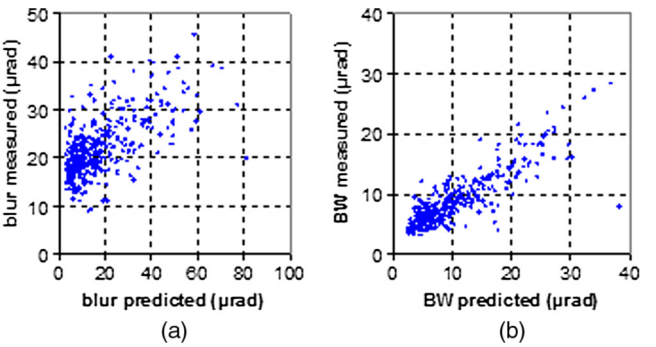

Fig. 22 A comparison between the measured and predicted blur is shown in (a) and for the beam wander in (b) for the selected data series collected during the whole FATMOSE period.

for C_n^2 values $<10^{-15}$ $m^{-2/3}$ (or $\sigma_a < 14$ μrad). On the other hand, the measured beam wander appears to be somewhat smaller than the predicted one, as shown in Fig. 22(b), while the correlation between both is rather good (correlation coefficient 0.88).

6 Conclusions

Thanks to the long duration (more than 10 months) of the FATMOSE campaign, a large amount of data have been collected of atmospheric parameters, having a direct impact on the range performance of electro-optical systems in a coastal environment. Statistics have been presented on weather parameters and the atmospheric transmission in a number of spectral bands and on turbulence induced blur, beam wander and scintillation, considered to be representative year-round. The benefit of using electro-optical sensors, operating at longer wavelengths, has been shown quantitatively. The False Bay area was a perfect coastal location, presenting most of the time wind from ocean directions with wind speeds up to 20 m/s.

A complication in the False Bay is the possibility of local variation in the water temperature due to the mixing of warm and cold ocean currents in the area. This may result in inhomogeneities of ASTD along the path. As a consequence, the temperature profiles in the marine boundary layer may vary, affecting the ray trajectories along the path. Also the fluxes of heat, momentum and moisture, governing the MO boundary layer structure, become variable, causing C_n^2 variations along the path. In a similar way it was observed that the

visibility (aerosol content) may vary locally due to the presence of fog patches.

The variability of the weather conditions did often occur in short time notices, which made it necessary to carefully select periods of several hours with constant weather for model validation. In this way an aerosol model, based upon a Junge particle size distribution, was proposed. Differences in aerosol transmission in the five spectral bands of the TNO multiband spectral radiometer transmissometer MSRT were used to successfully determine the Junge coefficients J_e and J_c. Of course, this method of retrieval fails in adverse weather conditions, such as low visibility and rain. The effect of wind speed as well as transmission level on J_e and J_c was illustrated, showing that both parameters increase with wind speed. Alternatively, both J_e and J_c were decreasing with increasing transmission level due to the associated decrease of relative humidity impacting the particle size distribution of the aerosols.

In a similar way, the environmental parameters were used as input for the TARMOS model, predicting the boundary layer structure, in particular the temperature profile and the structure parameter for the refractive index C_n^2. Another selection of events was chosen allowing the successful validation of the predicted logarithmic temperature profile for ASTD values between -2 and $+4$ K. This validation was carried out by using a high resolution theodolite (7.5 μrad pixel), providing absolute angle of arrival data from sources at NSRI. In addition, differential angles of arrival were measured from two vertically separated sources at NSRI by means of a high resolution telescope (5 μrad pixel).

The parameter C_n^2 was also locally measured in the Bay by means of a scintillometer, running over a 1.8 km path between IMT and RRL, and a sonic anemometer mounted at RRL. These sensors provided opportunities to validate the TARMOS prediction model on C_n^2 and associated models on scintillation, blur (short term) and beam wander. Because of the long range, the weak turbulence theory is not valid anymore for C_n^2 values 2×10^{-16} m$^{-2/3}$. For this reason, the strong turbulence theory was used to calculate the aperture averaging factor for the large-aperture long range scintillometers. Measured scintillation indices SI did compare very well with the predictions, based upon the C_n^2 data from the local scintillometer. Apparently, the SI was independent of wavelength, indicating that in this case, scintillation was mainly due to refraction effects of larger turbulence eddies and instead of diffraction by small eddies.

Scintillation spectra did show the expected shape according to the Kolmogorov theory, although the knee in the log-log scale was occurring at 10 Hz instead of 1 Hz. The mean value of the measured blur, which was of the order of 20 μrad, corresponds well with the predictions from the mean C_n^2. The blur was, however, staying too big for low C_n^2 values. It was further found that the blur values can vary considerably within one data series, the reason why occasionally "lucky shots" did occur with 50% less blur. Beam wander measurements did correlate quite well with the predictions, where it was found that for low C_n^2 values, the predictions corresponded better than with the blur.

It was shown that the value of the beam wander is generally about 40% of the blur value. The blur values have an impact on the resolution of sensors. First of all, the blur has to be translated to other ranges. Secondly, the blur, defined as the root of the geometrical mean of the variances of the intensity distribution for a point source in X- and Y-direction, has to be multiplied by a factor 2.43 in order to obtain the optical resolution. This factor results from the consideration of the separation of two line sources at such a distance that they are just discernible. A mean blur value of 20 μrad implies thus an optical resolution of 49 μrad, which corresponds to a distance of two point sources of 0.77 m at a range of 15.7 km.

Acknowledgments

The authors want to thank Michael Saunders (Station 16 Commander) and Mario Fredericks (Station 16 Deputy Commander) from the National Sea Rescue Institute for permission for mounting the sources on the building at Strandfontein and their support during the trial. Also IMT personnel, in particular Faith February and George Vrahimis, are greatly acknowledged for their support in keeping the system running and handling the data. At TNO, we thank Peter Fritz for his efforts in preparing the trial and installing the systems. Koen Benoist, Leo Cohen, Koos van der Ende and Marco Roos are acknowledged for preparing hardware and software for data acquisition and analysis.

References

1. C. D. O'Dowd and G. de Leeuw, "Marine aerosol production: a review of the current knowledge," *Phil. Trans. R. Soc. A* **365**, 1753–1774 (2007).
2. F. X. Kneizis et al., "The MODTRAN 2/3 report and Lowtran 7 model," Phillips Laboratory, Geophysics Directorate, PL/GPOS, Hanscom AFB, MA (1996).
3. S. P. Arya, "Introduction to Micrometeorology," *International Geophysics Series*, Vol. **79**, Academic Press, London (2001).
4. L. C. Andrews and R. L. Philips, *Laser Beam Propagation through Random Media*, 2nd ed., SPIE Press, Bellingham (2005).
5. G. C. Holst, *Electro-Optical Imaging System Performance*, 3rd ed., Vol. 121, SPIE Press, Bellingham (2003).
6. A. N. de Jong et al., "Application of year-round atmospheric transmission data, collected with the MSRT multiband transmissometer during the FATMOSE trial in the False Bay area," *Proc. SPIE* **8161**, 81610A (2011).
7. A. N. de Jong et al., "Marine boundary layer investigations in the False Bay, supported by optical refraction and scintillation measurements," *Proc. SPIE* **8178**, 817808 (2011).
8. A. N. de Jong et al., "Long-term measurements of atmospheric point spread functions over littoral waters, as determined by atmospheric turbulence," *Proc. SPIE* **8355**, 83550M (2012).
9. A. N. de Jong et al., "Characteristics of long-range scintillation data over maritime coastal areas," *Proc. SPIE* **8535**, 853504 (2012).
10. H. C. van de Hulst, *Light Scattering by Small Particles*, Dover Publications, Inc., New York (1981).
11. A. N. de Jong et al., "Atmospheric refraction effects on optical/IR sensor performance in a littoral-maritime environment," *Appl. Opt.* **43**(34), 6293–6303 (2004).
12. R. R. Beland, "Propagation through atmospheric optical turbulence," *The Infrared & Electro-Optical Systems Handbook*, Vol. 2, SPIE, Bellingham (1993).
13. T.-i Wang, G. R. Ochs, and S. F. Clifford, "A saturation-resistant optical scintillometer to measure C_n^2," *JOSA* **68**(3), 334–338 (1978).
14. R. J. Hill and G. R. Ochs, "Fine calibration of large-aperture optical scintillometers and an optical estimate of inner scale of turbulence," *Appl. Opt.* **17**(22), 3608–3612 (1978).
15. A. N. de Jong, E. M. Franken, and J. Winkel, "Alternative measurement techniques for infrared sensor performance," *Opt. Eng.* **42**(3), 712–724 (2003).
16. D. L. Fried, "Optical resolution through a randomly inhomogeneous medium," *JOSA* **56**, 1372–1379 (1966).

Biographies and photographs for all authors are not available.